Nanoindentation measurements of the mechanical properties of polycrystalline Au and Ag thin films on silicon substrates: Effects of grain size and film thickness

Yifang Cao [a,*], Seyed Allameh [a], Derek Nankivil [b], Steve Sethiaraj [c], Tom Otiti [d], Wole Soboyejo [a]

[a] *Princeton Institute for the Science and Technology of Materials (PRISM) and Department of Mechanical and Aerospace Engineering, Princeton University, Princeton, NJ 08544, United States*
[b] *Department of Mechanical, Materials and Aerospace Engineering, University of Central Florida, 4000 Central Florida Boulevard, Orlando, FL 32816, United States*
[c] *Department of Physics, University of Botswana, Private Bag UB 0022, Gaborone, Botswana*
[d] *Department of Physics, Makerere University, Kampala, Uganda*

Received 8 February 2006; accepted 22 April 2006

Abstract

This paper presents the results of nanoindentation experimental studies of the contact-induced deformation in Au and Ag thin films. The paper examines the effects of film thickness and substrate deformation restraint on the mechanical properties of electron beam (e-beam) deposited Au and Ag films. Following a brief description of film microstructure, surface topography, and contact-induced pile-up deformation, film mechanical properties (hardness and Young's modulus) were determined using nanoindentation techniques. The indentation size effects (ISE) observed in films with different thicknesses were explained using a mechanism-based strain gradient (MSG) theory. The intrinsic film yield strengths and hardnesses extracted from the MSG theory are shown to exhibit classical Hall–Petch dependence on the inverse square root of the average film grain size. Displacement bursts were also found to occur in Ag films at indentation load levels of 100 μN. These were attributed to the initial onset of dislocation slip activity, when the shear stress exceeds the estimated theoretical shear strengths of the materials.

Keywords: Nanoindentation; fcc thin films; Hardness; Young's modulus; Hall–Petch effects; Thickness effect

1. Introduction

In recent years, significant efforts have been made to develop microelectronics and microelectro-mechanical systems (MEMS) structures in which face-centered cubic (fcc) films have been used as metallic contacts at the micro- and nano-scales [3–5]. However, the physics of contact-induced deformation of fcc films has not been fully investigated, since the mechanical properties of the small structures may be significantly different from those of bulk materials [6].

The differences between the mechanical properties of small structures and bulk materials may be attributed to: differences in microstructure due to the fabrication [6]; possible substrate effects on thin films [1,2,7,8] and film size effects due to strain gradient plasticity phenomena [9–11]. There is, therefore, a need to study the mechanical properties of fcc films at the appropriate scale.

A number of experimental researchers [12–15] have made efforts to study the nano/micro-scale mechanical properties of polycrystalline fcc metals. However, a complete understanding of mechanical properties of fcc films is yet to emerge. In particular, there is a need to develop a basic understanding of the effects of film thickness, microstructure and substrate modulus.

This paper presents the results of an experimental study of the effects of film microstructure/thickness on contact-induced deformation in polycrystalline Au and Ag thin films produced by electron-beam deposition on silicon substrates. Following a brief description of sample preparation and surface microstructure, contact-induced material pile-up and film mechanical properties (hardness and Young's modulus) are characterized using

* Corresponding author. Fax: +1 609 258 5877.
E-mail address: yifangc@princeton.edu (Y. Cao).

nanoindentation techniques. The effects of Au and Ag film thicknesses and microstructure on indentation size effects (ISE) are analyzed within the framework of the mechanism-based strain gradient (MSG) theory.

The intrinsic yield stress/hardness, extracted from the MSG theory, is shown to exhibit a Hall–Petch dependence on grain size. The strengthening increase with decreasing film thickness is also explained by the measured microstructural length scales obtained from the MSG theory. Subsequently, Young's moduli are determined using the conventional Oliver–Pharr method and models by King [1], and Saha and Nix [2] that account for substrate effects. Finally, displacement bursts are observed to occur when the shear stress underneath the indenter just exceeds the theoretical shear strength of the material.

2. Theory

Doerner and Nix [7], and later on Oliver and Pharr [16,17] developed a most comprehensive method for determining the hardness and modulus from depth sensing indentation (DSI) load–displacement data. In the theory, the Meyer's definition of hardness, H was adopted. This is given by:

$$H = \frac{P_{\max}}{A} \tag{1}$$

where $P_{\max}$ is the maximum load and A is the projected contact area. The recorded load–displacement data were used to relate the stiffness, S, from the slope of the initial unloading curve, to the reduced elastic modulus, E_r:

$$E_r = \frac{\sqrt{\pi}}{2}\frac{S}{\sqrt{A}} \tag{2}$$

where S is the contact stiffness corresponding to the slope of the load–penetration curve at the beginning of the unloading, and E_r is expressed in terms of the elastic moduli (E) and Poisson's ratios (ν) of the indenter (i) and the indented material (im):

$$\frac{1}{E_r} = \frac{1-\nu_i^2}{E_i} + \frac{1-\nu_{im}^2}{E_{im}} \tag{3}$$

In the case of film/substrate systems, the indentation response is a combined elastic–plastic response from the film and the substrate. A solution can be found from Saha and Nix [2] to decouple the combined indentation response from the film and the substrate, and extract the intrinsic mechanical properties of the film. Their modified solution assumes that a flat punch is situated at the tip of the indenter. This yields:

$$\frac{1}{E_r} = \frac{1-\nu_i^2}{E_i} + \frac{1-\nu_f^2}{E_f}(1-e^{-\alpha(t-h)/\sqrt{A}}) + \frac{1-\nu_s^2}{E_s}(e^{-\alpha(t-h)/\sqrt{A}}) \tag{4}$$

where t is the film thickness, E_f and ν_f are the modulus and Poisson's ratio of the film, E_s and ν_s are the modulus and Poisson's ratio of the substrate, α is a numerically determined scaling parameter that is a function of indentation size [1,2] and can be determined from expressions in Ref. [2].

For a Berkovich tip, the projected contact area A has a calibrated relationship with the contact depth h_c. This is given by [16]:

$$A(h_c) = 24.5h_c^2 + C_1h_c^1 + C_2h_c^{1/2} + \cdots + C_8h_c^{1/128} \tag{5}$$

where C_1 through C_8 are constants. The first term on the right describes a perfect Berkovich indenter, the others describe the deviations from the ideal Berkovich geometry due to blunting [11] at the tip. The blunting distance ξ can be calculated from the actual geometry of the tip and the reference tip radius provided by tip manufacturer. For the Berkovich tip that was used in this study, the blunting distance is calculated to be 5.7 nm.

In some materials, the volume deformed under the indenter pushes out into the sides of the indenter forming a pile-up profile [2,18]. Due to this pile-up shape, the actual contact depth is larger than the measured contact depth h_c, the difference can be estimated as the pile-up height h_p. Hence, the calculated projected area based on the recorded h_c will underestimate the contact area. Thus, the material pile-up effect must be corrected to obtain the true properties. This is done by measuring the pile-up height, h_p, associated with each indent, and adding it to the measured h_c.

After the tip rounding distance ξ [11] and indentation pile-up height h_p [2] are taken account, the corrected contact area is given by:

$$A(h_c) = 24.5(h_c+\xi+h_p)^2 + C_1(h_c+\xi+h_p)^1 + C_2(h_c+\xi+h_p)^{1/2} + \cdots + C_8(h_c+\xi+h_p)^{1/128} \tag{6}$$

For contact-induced deformation in the micro- and nano-scale regimes, the hardness increases as the indentation size decreases, in metallic materials [9–11]. This so-called indentation size effect has been explained recently using the mechanism-based strain gradient (MSG) plasticity theory, established by Nix and Gao [9]. This gives:

$$\frac{H}{H_0} = \sqrt{1+\frac{h^*}{h}} \tag{7}$$

where h is the depth of indentation, H_0 is the plateau hardness in the limit where there are no strain gradient effects and h^* is a characteristic length scale that depends on the shape of indenter, the shear modulus and H_0. This model was used to derive the following law for strain gradient plasticity:

$$\left(\frac{\sigma}{\sigma_0}\right)^2 = 1 + \hat{l}\chi \tag{8}$$

where σ is the effective flow stress in the presence of a gradient, σ_0 the flow stress in the absence of a gradient, χ the effective strain gradient and $\hat{l}$ is a characteristic material length scale. Note that $\hat{l}$ can be expressed in terms of the Burger's vector b and shear modulus μ [11]. This gives:

$$\hat{l} = \frac{b}{2}\left(\frac{\mu}{\sigma_0}\right)^2 \tag{9}$$

Hence, the length scale $\hat{l}$ can be thought of as a formalism that enables the strain contributions to plasticity from strain gradients to be modeled within a continuum framework. For the case of pure fcc metals, this length scale positively increases with the mean spacing between statistically stored dislocations (SSD) L_s, through the following expression [9]:

$$\hat{l} = \frac{4}{3}\frac{L_s^2}{b} \tag{10}$$

The yield strength of polycrystalline materials, σ_0, is also affected by the grain size. The grain size dependence is given by this well-known Hall–Petch relationship [19]. This gives the following:

$$\sigma_0 = \sigma_{0i} + \frac{k_y}{\sqrt{d}} \tag{11}$$

where d is the grain size, σ_{0i} the intrinsic yield strength in the absence of grain size effects and k_y is a material constant.

3. Materials

3.1. Sample preparation

Polycrystalline Au and Ag thin films with different thickness were deposited onto substrates of Si. The Si substrates were obtained from Silicon Quest International Company, Santa Clara, CA. Prior to deposition, the silicon wafers were prepared by submerging them in a 4:1 mixture of sulfuric acid and hydrogen peroxide in order to clean the wafer. They were then rinsed in hydrofluoric acid to remove the remaining oxide layer, before rinsing with water to remove any residual impurities. Subsequently, the Au or Ag films were deposited on the silicon wafers using a Denton/DV-502A E-Beam Evaporator (Denton Vacuum, Moorestown, NJ) that was operated at pressures below 10^{-6} Torr, and a substrate temperature below 40 °C. A deposition rate of 0.5 nm/s was used. In this way, Au and Ag thin films with thicknesses of 100, 500, 1000 and 2000 nm were produced.

3.2. Microstructure and surface topography

The microstructure and surface topographies of the as-deposited films were examined using a Dimension 3100 atomic force microscope (AFM) (Veeco Instruments, Woodbury, NY). The AFM was operated in the tapping mode. Typical AFM images of the films with thicknesses of 100, 500, 1000 and 2000 nm deposited on the silicon substrates are presented in Fig. 1. The AFM images show the equiaxed grain structures in the as-deposited films. The grain size data that were obtained for the Au and Ag films were summarized in Table 1. The results show the average grain size of both the Au and Ag films increased with increasing film thickness, increasing from approximately 20 nm, for the 100 nm thick Au film and 40 nm, for the 100 nm thick Ag film, to 130 nm, for the 2000 nm thick Au film and 160 nm, for the 2000 nm thick Ag film. The results are, therefore, consistent with prior studies of other metal film microstructure

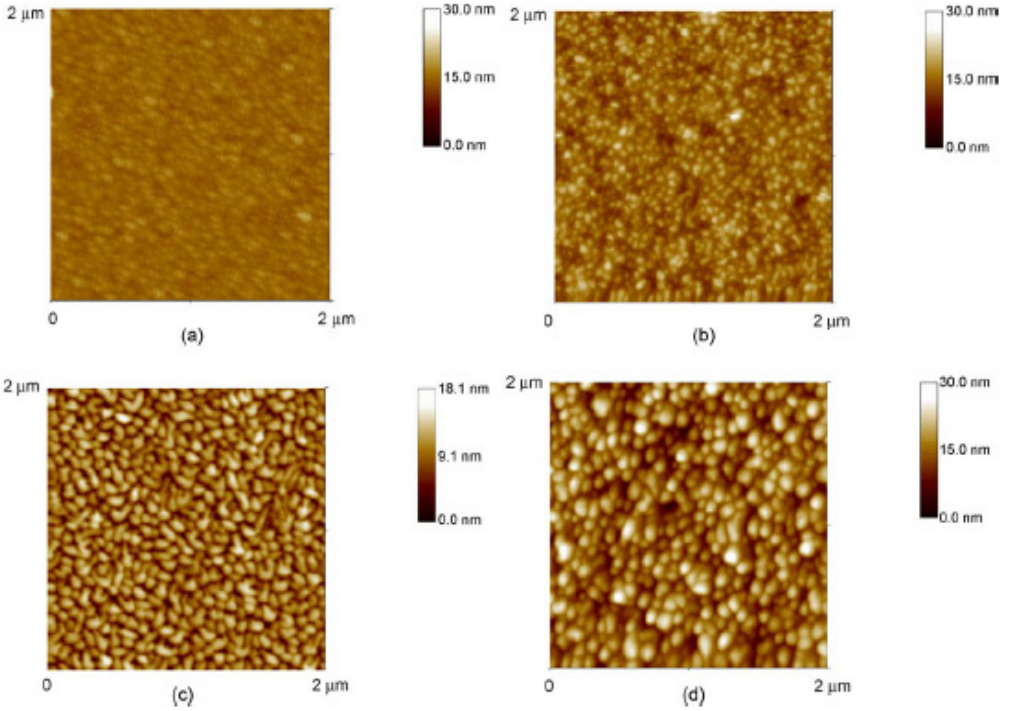

Fig. 1. AFM images of surface topography of Au films on silicon substrates prepared by e-beam evaporation with film thickness 100 nm (a), 500 nm (b), 1000 nm (c) and 2000 nm (d).

Table 1
Grain sizes obtained for the Au and Ag films using atomic force microscopy scans

Film thickness (nm)	Au film grain size (nm)	Ag film grain size (nm)
100	21	41
500	39	97
1000	76	142
2000	126	159

[20–22], which show that grain size increases with increased film thickness.

It was also found that most of the grains in the as deposited Au film have a (1 1 1) orientation, using electron back-scattered diffraction (EBSD) techniques [23]. Similar results have been obtained for other face-centered cubic (fcc) films deposited on a range of substrates [24–26].

4. Experimental techniques and calibrations

The measurements of hardness and modulus were performed using a TriboScope (Hysitron Inc., Minneapolis, MN) Nanomechanical Testing System integrated with a DI Dimension 3100 AFM frame. A three-plate capacitive transducer was used by the TriboScope system to control the applied load and displacement. The low spring mass (200 mg) of the transducer's center plate minimized the instrument's sensitivity to external vibrations. Within the system, the standard cantilevered AFM tip was replaced with a diamond indenter. This served as both the indenter probe and an imaging probe, thereby eliminating any uncertainty in locating the indentation after unloading.

A Berkovich (three-sided pyramid tip, 142.3°) diamond indenter was used in this study. Peak loads, ranging between 100 and 11,000 μN were explored for different film/substrate systems. The loading profiles included three segments: loading to a peak load; holding at the peak load; unloading back to the zero load. Loading and unloading rates of 400 μN/s were applied. A holding period of at least 3 s was applied to allow time-dependent effects to diminish.

Only regions with relatively low roughness values were chosen for performing the indentations. Hence, the possible effects of rough surfaces (on the hardness and modulus measurements) were minimized. Furthermore, in an effort to decrease the possible interactions between adjacent indents, all the indents were separated by 5–10 μm. During the test, the surfaces were imaged with a contact-based scanning probe technique with the indenter tip before and after each indentation. A load–displacement curve was also recorded for each indent.

After the indentation tests, the load–displacement curves obtained for the different indents were mapped onto the same master (load–displacement) curve. Fig. 2 shows the typical load–displacement curves obtained for the different indents on the same sample. For consistency, only load–displacement profiles that mapped onto the same master curve were admitted as valid measurements (the invalid profiles have a fraction less than 5% for each film we tested).

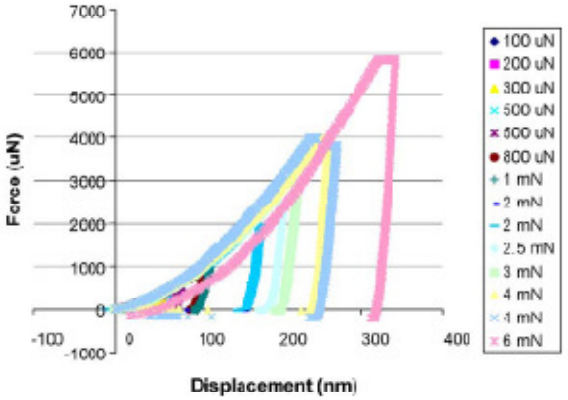

Fig. 2. The load–penetration curves obtained from the nanoindentation experiments performed to different loads on the 500-nm-thick Au film on Si substrate.

The tip area function was calibrated by indenting on fused quartz sample, following the approach suggested by [16,27]. With a constant modulus assumption for the standard fused quartz sample from Hysitron Inc., Minneapolis, MN (Young's modulus of 72 GPa), the projected contact area A was calculated for each indent based on Eq. (2). Then, a plot of the computed area A as a function of contact depth h_c was plotted in Fig. 3 and a fitting procedure was employed to fit the A versus h_c to a polynomial form (Eq. (5)). Using this approach, the coefficients C_1 through C_8 have been calibrated for the Berkovich indenter used in the current study.

As a control, nanoindentation experiments were also performed on silicon substrates. These were used to check the performance of the indentation system, as well as to provide the baseline data for our films on Si substrates. Young's modulus, hardness, and the indented profile obtained for the Si substrate are presented in Fig. 4. Clearly, Fig. 4(a) shows that there is no significant pile-up on the Si substrate. The silicon moduli and hardness values are calculated to be independent of indentation depth, as shown in Fig. 4(b), with the average Young's modulus of 181 ± 12 GPa and the average hardness of 10.2 ± 0.8 GPa,

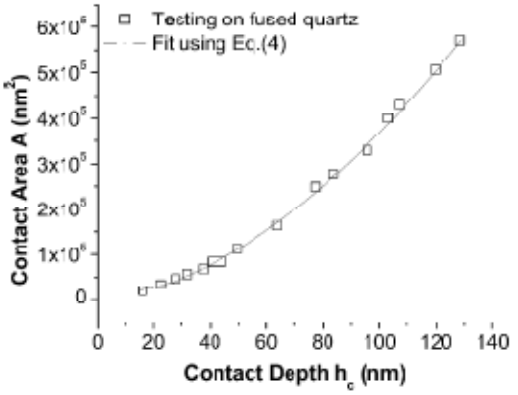

Fig. 3. The computed projected contact area A as a function of contact depth h_c with a polynomial fit (Eq. (5)).

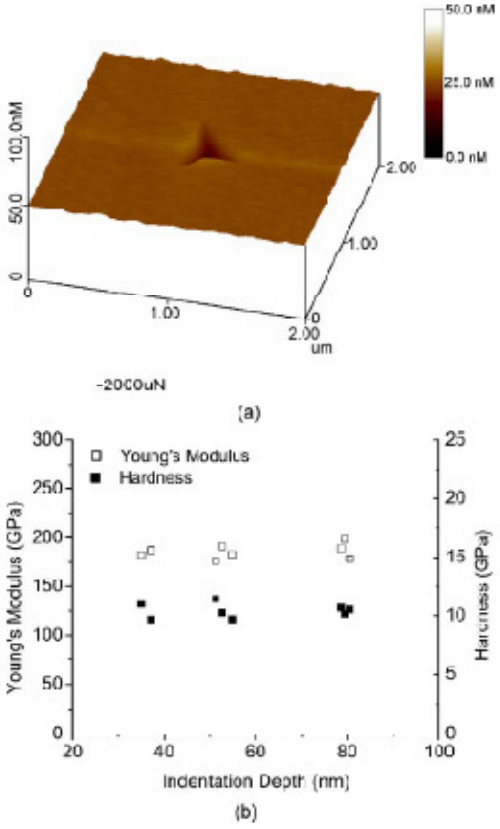

Fig. 4. The indented profile in (a), Young's modulus and hardness in (b) obtained for the Si substrate.

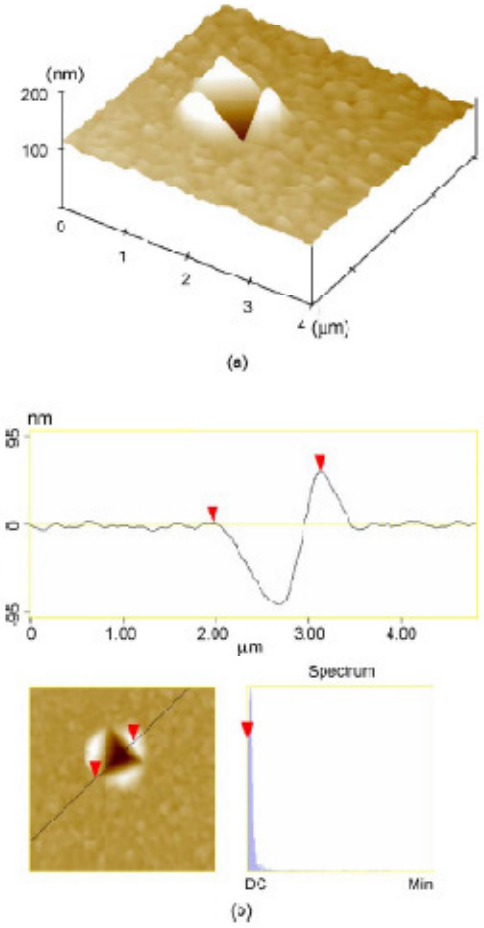

Fig. 5. Significant material pile up was observed. (a) A typical AFM image taken after a nanoindentation test on a Au film on Si substrate shows significant pile-up. (b) Typical section analysis performed for a pile-up AFM image taken after a nanoindentation test.

which are in good agreement with the values obtained from Ref. [2]. These values were useful for determining the actual film properties using the modified King's model [1,2]. The absence of a significant size effect on the hardness of the silicon substrate is attributed to the limited plasticity in silicon.

5. Results and discussion

5.1. Materials pile-up

Significant material pile-up was found to occur in the fcc polycrystalline Au and Ag thin films with different thicknesses. Typical images showing pile-up as well as the relevant section analysis are presented in Fig. 5(a) and (b), respectively. The pile-up is due to the severe constrained plastic deformation in the films.

The extent of material pile-up increases monotonically with increasing indentation depth and increasing film thickness (Fig. 6(a)). It is important to note that, without appropriate correction, this significant pile-up (as high as 20% of the indentation depth at high loads) could cause an underestimation of the contact area deduced from Oliver–Pharr method [2]. Hence, the material pile up effect has to be accounted for in determining the contact area in Eq. (5). The effects of material pile-up were accounted for in the current analysis of the data, following the approach in [2,11], as described in Section 2.

It was also observed that thinner films get higher pile-up when subjected to the same indentation load. For example, the AFM images obtained after nanoindentations at 500 μN on Ag films with thicknesses of 100 and 1000 nm were presented in Fig. 6(b) and (c), respectively. They clearly show that pile-up deformation diminishes in thicker films. This trend was also observed for Au films. It could be due to the relatively more severe constrained plastic deformation in thinner films, since pile-up is due to the severe constrained plastic deformation in the films [2].

5.2. Hardness and yield strength

The hardness values obtained for Au and Ag films of different thickness (versus normalized indentation depth) are presented

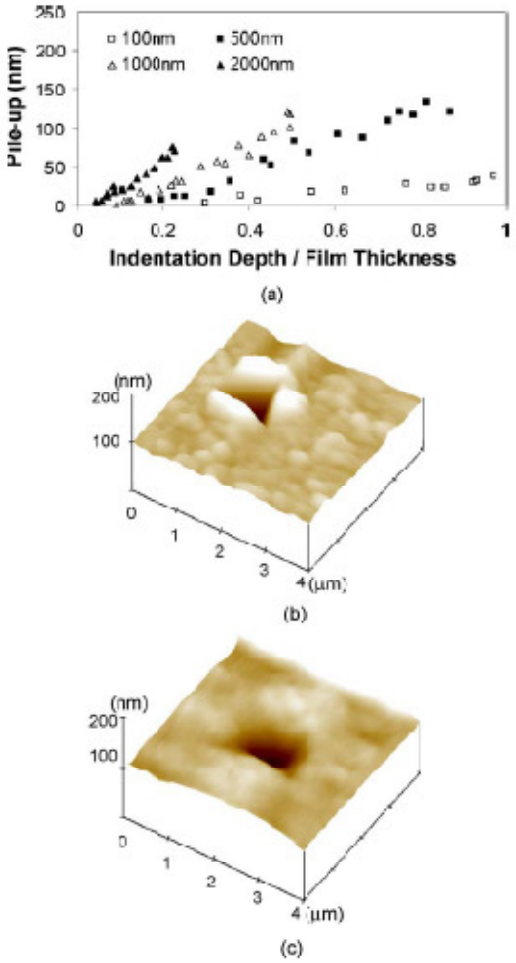

Fig. 6. Pile-up height changes with normalized indentation depth for different Ag film thicknesses in (a), typical pile-up AFM images obtained for 100 nm thick Ag film in (b) and 1000 nm thick Ag film in (c), subjected to the same indentation load (500 μN).

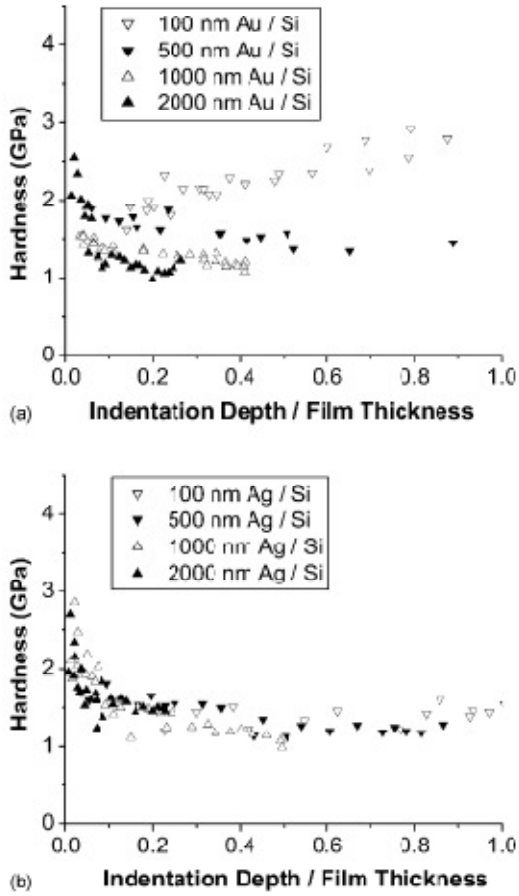

Fig. 7. Film thickness effect on hardnesses of Au films in (a) and Ag films in (b).

in Fig. 7. For the thinnest film (film thickness of 100 nm), the measured hardness values increase with increasing indentation depth. This increase is attributed largely to the effects of substrate modulus mismatch. The usual indentation size effects are observed for indents with depth to film thickness ratios of up to ~0.2 for the thicker films (film thickness of 500, 1000 and 2000 nm). This is attributed largely to the effects of geometrically necessary dislocations at small scales [9]. This critical ratio of 0.2, below which the indentation size effect can be well captured by the effects of geometrically necessary dislocations [9], matches well with the critical ratio of 0.18–0.22 measured for the Au films on Ni substrates [12].

The depth independent hardnesses, H_0, for different film thickness can be taken as the hardnesses in the absence of geometrically necessary dislocations. This can be obtained by fitting Eq. (7) to the experimental data. The hardness values obtained using this method are summarized in Table 2. This shows that the hardnesses decrease with increasing Au film thickness, from approximately 1.6 GPa for 500 nm thick Au and Ag films, to 1.1 GPa for 2000 nm thick Au film and 1.5 GPa for 2000 nm thick Ag film. Since the film grain size increases with increasing film thickness (Table 1), an effort was made to relate the film grain size to the intrinsic film strength/hardness in the absence of SGP

Table 2
List of the intrinsic hardness H_0 in the limit of infinite depth for different film thickness (500, 1000, 2000 nm) and the corresponding microstructural length scales

Sample specifications	b (nm)[a]	μ (GPa)[a]	H_0 (GPa)	l (μm)
Au				
500 nm	0.2885	30.4	1.58	0.48
1000 nm	0.2885	30.4	1.27	0.74
2000 nm	0.2885	30.4	1.06	1.07
Ag				
500 nm	0.2892	33.6	1.63	0.55
1000 nm	0.2892	33.6	1.57	0.60
2000 nm	0.2892	33.6	1.51	0.64

[a] Ref. [40].

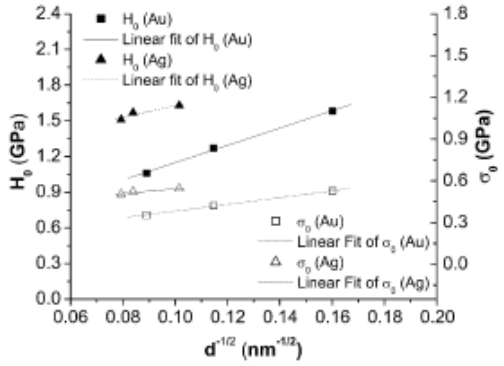

Fig. 8. Plots of H_0 vs. $d^{-1/2}$ and σ_0 vs. $d^{-1/2}$ with the corresponding linear fit for Au and Ag films.

phenomena. Since the intrinsic hardness, H_0, corresponds to a large indent, the intrinsic yield strength can be estimated from Tabor's relation [9] which gives $H_0 = 3\sigma_0$. Hence, the Hall–Petch relation (Eq. (11)) can be expressed as:

$$H_0 = 3\sigma_0 = 3\sigma_{0i} + \frac{3k_y}{\sqrt{d}} \tag{12}$$

Fig. 8 shows the experimental data of H_0 and σ_0 versus $d^{-1/2}$ as well as the corresponding linear fits based on Eq. (12). The correlation coefficients of the linear fits are above 0.95. Since Eq. (12) relies on the linear Tabor's relation, $\sigma_0 = H_0/3$, so H_0 can be linearly related to $d^{-1/2}$. The values of k_y and σ_{0i} obtained using the linear fitting for Au films are 2.4 GPa $(nm)^{1/2}$ and 0.14 GPa, respectively. These are comparable to the reported Hall–Petch coefficients of ~3 GPa $(nm)^{1/2}$ for Au films [28] and the reported yield strengths ~0.2 GPa for Au bulk material and thin films [6,29,30]. The values of k_y and σ_{0i} obtained using the linear fitting for Ag films are 1.6 GPa $(nm)^{1/2}$ and 0.38 GPa, respectively. These are comparable to the reported Hall–Petch coefficients of 1.0–1.5 GPa $(nm)^{1/2}$ for Ag films [31] and the reported yield strengths 0.1–0.2 GPa for Ag thin films [31]. Hence, the method presented in this section provides a simple approach for the estimation of the intrinsic yield strength.

The material microstructure length scale $\hat{l}$ can be thought of as a formalism that enables the strain contributions to plasticity from strain gradients to be modeled within a continuum theory framework (Eq. (8)). Table 2 lists the material length scales obtained for Au and Ag films. Note that the material length scale is comparable to the film thickness, for the range of film thicknesses that were examined in the current work. The measured values of $\hat{l}$ were on the order of 1 μm. These are close to the ~1 μm values reported by Begley and Hutchinson [32] for a range of single crystals (Cu, Ag and W). Hence, the measured values of $\hat{l}$ are consistent with prior reported values. However, the material length scales also increase with increasing film thickness, for films with thicknesses between 500 and 2000 nm. Based on Eq. (10), larger values of $\hat{l}$ in thicker films indicate greater spacing between statistically stored dislocations. This could lead to weaker dislocation interactions and lower intrinsic strengthening levels in films with increased thicknesses. This is consistent with our current experimental results (Table 2), which show thicker films have significantly lower intrinsic hardness values.

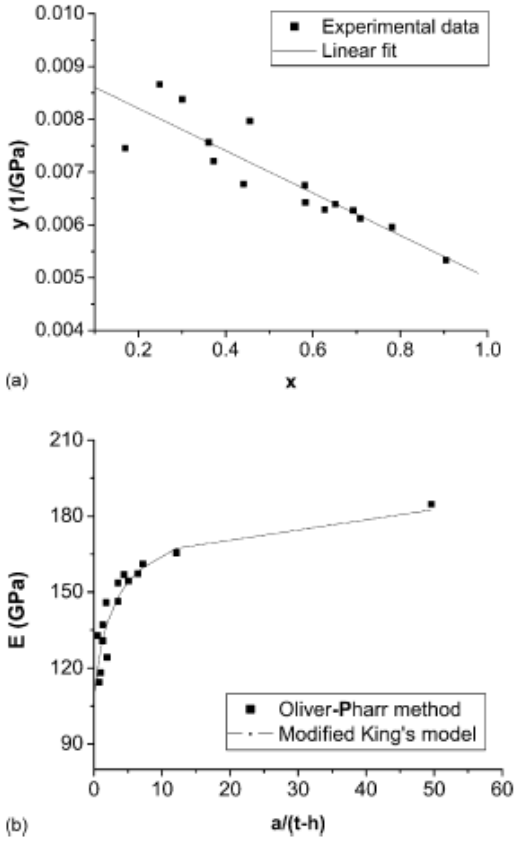

Fig. 9. Young's modulus determination for nanoindentation tests. (a) A plot of $y = \left(\frac{1}{E_r} - \frac{1-\nu_i^2}{E_i}\right)\frac{1}{1-\nu_f^2}$ vs. $x = e^{-\alpha(t-h)/\sqrt{A}}$ for a 500-nm-thick Au film on a (1 0 0) silicon substrate. (b) The Young's modulus data obtained using the Oliver–Pharr method and a fit using the modified King's model.

5.3. Young's modulus

Young's moduli of the Au and Ag thin films were obtained using the modified King's model [2] to account for substrate effects. Eq. (4) corresponds to the equation for a straight line $y = Ax + B$, where

$$x = e^{-\alpha(t-h)/\sqrt{A}}, \qquad y = \left(\frac{1}{E_r} - \frac{1-\nu_i^2}{E_i}\right)\frac{1}{1-\nu_f^2},$$

$$A = \frac{1-\nu_s^2}{E_s(1-\nu_f^2)}, \qquad B = \frac{1}{E_f}$$

By plotting the values of y versus x, the constants A and B can be determined using the least squares method. A typical plot of y versus x (with linear fitting) is presented in Fig. 9(a). Fig. 9(b) shows a typical plot of Young's modulus versus the normalized

Table 3
The Young's modulus values for Au and Ag films of different thicknesses on silicon substrates

	Film thickness (nm)			
	100	500	1000	2000
Au film Young's modulus (GPa)	105	111	94	105
Ag film Young's modulus (GPa)	85	86	112	95

indentation depth. The Oliver–Pharr method (Eq. (3)) was used to calculate the combined elastic modulus, while the modified King's method (Eq. (4)) was used to extract the film modulus.

The values of E_f obtained for the Au and Ag films (of different thicknesses) on silicon substrates are summarized in Table 3. In the analysis, diamond indenter properties E_i and ν_i were taken as 1140 GPa and 0.07, respectively [2]. The Poisson's ratio of both the film and substrate was assumed to be 0.3 since it has a minor effect on the indentation results [2]. The Young's moduli for the Au films of different thickness are between 94 and 111 GPa. These are close to the Young's modulus of 117 GPa expected for ⟨1 1 1⟩ orientated bulk Au single crystals ($E_{1\,0\,0}$ = 43 GPa and $E_{1\,1\,0}$ = 81 GPa) [33]. Since a ⟨1 1 1⟩ film texture was observed in the EBSD experiments we conducted, the measured moduli are consistent with expectations. The measured Young's moduli here reasonably agree with the moduli of 79–150 GPa reported in [12] for Au films on Ni substrate with film thicknesses between 300 and 5120 nm. The Young's moduli for the Ag films of different thickness are between 85 and 112 GPa. These are close to the Young's modulus expected for ⟨1 0 0⟩ orientated bulk Ag single crystals ($E_{1\,0\,0}$ = 124 GPa, $E_{1\,1\,0}$ = 243 GPa and $E_{1\,1\,1}$ = 358 GPa) [33].

5.4. Dislocation bursts

A significant horizontal displacement jump was observed in the load–displacement curves of Ag thin films (Fig. 10). The initial horizontal jump occurred at loads between 30 and 37 μN. Similar displacement jumps have been observed by Corcoran and Colton [34] for single crystal Au, Gouldstone et al. [35] for polycrystalline and single crystal Al, and Suresh et al. [36] for copper thin films. They are generally believed to be due to the strain bursts that correspond to the onset of significant

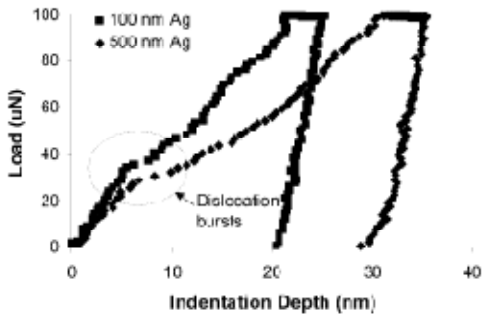

Fig. 10. Dislocation bursts observed on the load–penetration curves in Ag thin films on Si substrates with a maximum load of 100 μN.

Table 4
Material constants for Ag thin films with displacement bursts

for films	E_s (GPa)	ν_s	E_r (GPa)	τ_{max} (GPa)	τ_{th} (GPa)
100 nm Ag	85	0.37	91	5.5–5.6	5.3
500 nm Ag	86	0.37	92	5.3	5.3

dislocation nucleation activity underneath the indenter [34–36]. The initial contact of the indenter can be considered to involve a spherical contact up to a specific transition indentation depth h_t [37]. This transition depth can be calculated using a simple geometric relationship as in [35]:

$$h_t = R(1 - \sin\alpha) \tag{13}$$

where α is the half included angle of the Berkovich tip (65.35°) and R is the tip radius. For the Berkovich tip used in the current study, R is about 100 nm, h_t can be calculated to be about 9 nm. Therefore, when the penetration depth is below 9 nm, the contact problem may be idealized as a Hertzian contact between a spherical indenter and a flat surface. We can see that the initial displacement bursts occurred at indentation depths between 6 and 9 nm, they extended to only several nanometers. Thus, the contact problem before the initiation of the displacement bursts can be considered as the contact between the spherical indenter and flat sample surfaces.

From contact mechanics [38], the maximum elastic shear stress underneath a spherical indenter is given by:

$$\tau_{max} = 0.31\left(\frac{6PE_r^2}{\pi^3 R^2}\right)^{1/3} \tag{14}$$

where P is the indentation load. The reduced modulus, E_r, is given by Eq. (3) [16]. For the diamond Berkovich tip, E_i is about 1140 GPa and ν_i is 0.07 [35]. The relevant moduli and Poisson's ratios of the samples were summarized in Table 4. The maximum shear stress underneath the indenter calculated using above data were also summarized in Table 4. Also included in Table 4 is the theoretical shear strength, τ_{th}, estimated from $\mu/2\pi$, where μ is the shear modulus. The estimated values of the theoretical shear strengths, τ_{th} = 5.3 GPa, for Ag films, are comparable to the maximum shear stresses of 5.3–5.6 GPa underneath the indenter that were obtained for Ag films (Table 4). Therefore, the agreement between τ_{max} and τ_{th} suggests that the displacement bursts occur when the shear stress underneath the indenter just exceeds the theoretical shear strength of the material. Hence, the displacement bursts are attributed to the onset of dislocation nucleation in the region of high stress underneath the indenter. Similar strain bursts have been reported by other researchers for Au [39], Cu [36] and Al [35] crystals. Some of these researchers also suggest that the onset of the strain bursts corresponds to the nucleation of dislocation activity. However, further work is needed to determine how dislocations nucleate, propagate and interact at stresses close to the theoretical shear strength.

6. Concluding remarks

This paper presents the results of an experimental study of the microstructure and mechanical properties of polycrystalline Au and Ag thin films on silicon substrates. The salient conclusions arising from this study are summarized below:

1. The grain sizes of the e-beam deposited Au and Ag films increase with increasing film thickness from 100 to 2000 nm.
2. The intrinsic hardnesses of the Au and Ag films decrease with increasing film thickness. The strengthening increase with decreasing film thickness can be reasonably well characterized by the Hall–Petch equation.
3. The measured microstructural length scales increase with increasing film thickness. This can also be used, at least partly, to explain the strengthening increase with decreasing film thickness, because smaller microstructural length scales correspond to smaller dislocation spacing and stronger dislocation interactions.
4. The Au and Ag film moduli extracted using the King model were 94–111 and 85–112 GPa, respectively. These are essentially independent of film thickness.
5. Displacement bursts occur in Ag films when the maximum shear stress underneath the indenter just exceeds the theoretical shear strength of the material. These are attributed to the nucleation of dislocations at stresses close to the theoretical shear strength.

Acknowledgments

This work was supported by the National Science Foundation (Grant Nos. DMR 0213706 and DMR 0231418). Appreciation is extended to the Program Managers (Dr. Ulrich Strom and Dr. Carmen Huber) for their encouragement and support. The authors would like to thank Ms. Zong Zong for useful technical discussions, Prof. Jeffrey Kysar and Mr. Yong Gan for providing help with EBSD facilities at Columbia University.

References

[1] R.B. King, Int. J. Solids Struct. 23 (1987) 1657–1664.
[2] R. Saha, W.D. Nix, Acta Mater. 50 (2002) 23–28.
[3] S. Majumder, N.E. McGruer, G.G. Adams, P.M. Zavracky, R.H. Morrison, J. Krim, Sens. Actuators A: Phys. 93 (2001) 19–26.
[4] J. Plummer, M. Deal, P. Griffin, Silicon VLSI Technology: Fundamentals, Practice and Modeling, Prentice Hall, Upper Saddle River, NJ, 2000.
[5] Y. Cao, C. Kim, S.R. Forest, W.O. Soboyejo, J. Appl. Phys. 98 (2005), p. 033713-1.
[6] M. Gadelhak, The MEMS Handbook, CRC Press, New York, 2002.
[7] M.F. Doerner, W.D. Nix, J. Mater. Res. 1 (1986) 601–609.
[8] J. Menčik, D. Munz, E. Quandt, E.R. Weppelmann, M.V. Swain, J. Mater. Res. 12 (1997) 2475–2484.
[9] W.D. Nix, H. Gao, J. Mech. Phys. Solids 46 (1998) 411–425.
[10] Q. Ma, D.R. Clarke, J. Mater. Res. 10 (1995) 853–863.
[11] J. Lou, P. Shrotriya, T. Buchheit, D. Yang, W.O. Soboyejo, J. Mater. Res. 18 (2003) 719–728.
[12] Z. Xu, D. Rowcliffe, Surf. Coat. Technol. 157 (2002) 231–237.
[13] T.F. Smith, S. Zheng, Surf. Eng. 16 (2000) 143–146.
[14] H.D. Espinosa, B. Prorok, J. Mater. Sci. 38 (2003) 4125–4128.
[15] Y. Cao, Z. Zong, W. Soboyejo, Mater. Res. Soc. Symp. Proc. 875 (2005) O5.6.1.
[16] W.C. Oliver, G.M. Pharr, J. Mater. Res. 7 (1992) 1564.
[17] G.M. Pharr, W.C. Oliver, F.B. Brotzen, J. Mater. Res. 7 (1992) 613.
[18] K. McElhaney, J. Vlassak, W. Nix, J. Mater. Res. 13 (1998) 1300–1306.
[19] W.D. Callister, Materials Science and Engineering an Introduction, John Wiley & Sons Inc., New York, 2003.
[20] Y. Xiang, X. Chen, J.J. Vlassak, Mater. Res. Soc. Symp. Proc. 695 (2002) 189–194.
[21] J.F. Chang, H.H. Kuo, I. Leu, M.H. Hon, Sens. Actuators B: Chem. 84 (2002) 258–264.
[22] M. Aguilar, P. Quintana, A.I. Oliva, Mater. Manuf. Process 17 (2002) 57–65.
[23] M.N. Alam, M. Blackman, Proc. Roy. Soc. London A 221 (1954) 224–242.
[24] Y.S. Jung, Appl. Surf. Sci. 221 (2004) 281–287.
[25] S. Strehle, S. Menzel, H. Wendrock, J. Acker, K. Wetzig, Microsc. Microanal. 9 (2003) 272.
[26] X. Li, Z. Yang, Mater. Sci. Eng. B 106 (2004) 41–45.
[27] TriboScope Users Manual, Hysitron Inc., Minneapolis, MN, 2000.
[28] S. Sakai, H. Tanimoto, H. Mizubayashi, Acta Mater. 47 (1998) 211–217.
[29] J.H. Ahn, E.C. Jeon, Y. Choi, Y.H. Lee, D. Kwon, Curr. Appl. Phys. 2 (2002) 525–531.
[30] A. Stalder, U. Durig, Appl. Phys. Lett. 68 (1996) 637–639.
[31] H. Conrad, K. Jung, Mater. Sci. Eng. A 391 (2005) 272–284.
[32] M. Begley, J. Hutchinson, J. Mech. Phys. Solids 46 (1998) 2049–2068.
[33] W. Soboyejo, Mechanical Properties of Engineered Materials, Marcel Dekker Inc., New York, 2003.
[34] S. Corcoran, R. Colton, Phys. Rev. B. 55 (1997) 16057–16060.
[35] A. Gouldstone, H. Koh, K. Zeng, A. Giannakopoulos, S. Suresh, Acta Mater. 48 (2000) 2277–2295.
[36] S. Suresh, T. Nieh, B. Choi, Scripta Mater. 41 (1999) 951–957.
[37] Y. Cao, D. Yang, W.O. Soboyejo, J. Mater. Res. 20 (2005) 2004–2011.
[38] K. Johnson, Contact Mechanics, Cambridge University Press, Cambridge, UK, 1985.
[39] J. Kely, J. Houston, Phys. Rev. B 57 (1998) 12588–12594.
[40] T. Trimble, R. Cammarata, K. Sieradzki, Surf. Sci. 531 (2003) 8–20.